Supplementary Materials for

Hillslopes Record the Growth and Decay of Landscapes

Martin D. Hurst,* Simon M. Mudd, Mikael Attal, George Hilley

*Corresponding author. E-mail: mhurst@bgs.ac.uk

Published 23 August 2013, *Science* **341**, 868 (2013)
DOI: 10.1126/science.1241791

This PDF file includes:

Materials and Methods

Hillslope Model

The evolution of a one-dimensional hillslope follows:

$$\frac{d\zeta}{dt} = \rho^* U - E = \rho^* U - \frac{dq_s}{dx} \quad [S1]$$

such that surface elevation ζ changes through time t where U is surface uplift rate [L T^{-1}], ρ^* is the density ratio between bedrock and dry soil, E is erosion rate [L T^{-1}], x is distance along the hillslope and q_s is volumetric sediment flux per unit width [L^2 T^{-1}] (dimensions of [L]ength, [M]ass and [T]ime denoted with square brackets). Sediment flux in steep, soil mantled landscapes can be modeled using (*10, 11*):

$$q_s = \frac{-DS}{1-(S/S_C)^2} \quad [S2]$$

where D is a transport coefficient [L^2 T^{-1}], S is hillslope gradient [L L^{-1}] and S_C [L L^{-1}] is a critical hillslope gradient toward which sediment flux becomes infinite. This system can be nondimensionalized (as denoted by an asterisk superscript) (*7*):

$$\zeta^* = \zeta / (S_C L_H) \quad [S3a]$$

$$x^* = x / L_H \quad [S3b]$$

$$U^* = U\left(\frac{2\rho^* L_H}{DS_C}\right) \quad [S3c]$$

$$t^* = t\left(D / {L_H}^2\right) \quad [S3d]$$

Substituting Equation 2 into 1 and using these nondimensionalizing definitions leads to the following solution for hillslope form:

$$\frac{d\zeta^*}{dt^*} = -\frac{d}{dx}\left(\left[\frac{d\zeta^*}{dx^*}\right]\left[1-\left|\frac{d\zeta^*}{dx^*}\right|^2\right]^{-1}\right) + \frac{1}{2}U^* \quad [S4]$$

which we use to model the evolution of a 1D hillslope through time.

Topographic Analysis

Roering, et al. (*7*) provide steady state solutions (i.e. when the condition $U=E$ is satisfied) for the above model which allow derivation of non-dimensional erosion rate E^* which is proportional to E (Equation 3c). The solutions also predict E^* based on quantifiable

hillslope topographic metrics, namely hilltop curvature C_{HT} [L^{-1}], hillslope length L_H [L] and mean hillslope gradient S [L/L]:

$$E^* = E\left(\frac{2\rho^* L_H}{DS_C}\right) \quad \text{[S5a]}$$

$$E^* = \frac{2C_{HT}L_H}{S_C} \quad \text{[S5b]}$$

Dimensionless relief can be derived theoretically as a function of E^* and predicted from topography using S:

$$R^* = \frac{1}{E^*}\left\{\sqrt{1+\left(E^*\right)^2} - \ln\left(\frac{1}{2}\left[\sqrt{1+\left(E^*\right)^2}\right]\right) - 1\right\} \quad \text{[S6a]}$$

$$R^* = \frac{S}{S_C} \quad \text{[S6b]}$$

We use Equations 5b and 6b to quantify E^* and R^* from topographic data, selecting S_C = 0.8 so that the requirement $R^* < 1$ is met. Varying S_C does not change the overall distribution of E^* vs. R^* data derivbed from topography but will alter their absolute values. These metrics are expected to deviate from their steady-state predictions when a hillslope is undergoing a transient response to base-level change. Following Hurst, et al. (*2*) we located hilltops as the adjoining margins of drainage basins extracted at a range of stream orders. In DBPR we restricted our analysis to interfluves trending roughly perpendicular to SAF, so that the hilltops are likely to be experiencing similar erosion rates on both sides of the divide (Fig. 1a). Using a 0.25m digital elevation model, we calculated the aspect, gradient and curvature (Laplacian) of elevation from the coefficients of a 6-term quadratic surface fitted by least squares to all cells within a 2.5m window centered on the cell of interest. C_{HT} was sampled directly at hilltops then an aspect-driven, steepest descent trace was run from each hilltop pixel until a mask defining the channel network/valley fill was encountered. From this trace L_H and S were calculated (see Fig. S1).

DEM Preparation

There were two principal concerns when preparing a DEM for this analysis. Firstly, the raw LiDAR point cloud contained returns misclassified as ground originating from small shrubs bushes (Fig S2 and Fig S3). These were identified and preferentially smoothed. Secondly, hilltops on the Dragon's Back Pressure Ridge get extremely narrow (<2 m) where denudation is rapid, and so calculating reliable values for C_{HT} required analysis to check for scale dependency (Fig. S4).

We interpolated raw point cloud LiDAR returns (point density ~4 m^{-2}) to a 0.25 m^2 resolution grid using MCC-LiDAR (*13*). This algorithm identifies locations in the point cloud where returns coincide spatially and removes the highest of these points. We do not

use MCC-LiDAR to identify shrub vegetation since the algorithm is dependent on curvature, and hence has a tendency to misidentify sharp hilltops as vegetation. To remove bushes and shrubs, the gridded data was smoothed using a non-local means filtering algorithm (*14*). Filtering is based on the assumption of regularity; that in the neighbourhood of the pixel of interest there are neighbourhoods that should look similar and therefore these non-local neighbourhoods can be used to predict the value at the original pixel. A non-local approach to DEM smoothing is particularly appealing towards the goal of removing bushes/shrubs which can be considered positive, high frequency noise since unlike many filtering techniques it does not assume the noise is normally distributed, therefore we minimize smoothing of hilltops. Fig. S2 shows an example of the effect of the smoothing.

We justify interpolation to a 0.25 m^2 grid resolution by arguing that this allows the true location and elevations of point cloud data to be better spatially resolved in the gridded approximation of the surface. This fine resolution allows us to calculate curvature over smaller windows, which is essential for resolving the curvature of narrow hilltops. Typically topographic curvature is calculated over scales greater than the characteristic wavelength of high-frequency noise associated with surface roughness, for example due to pit-mound topography generated by tree throw (*15*). At DBPR positive surface noise associated to low relief vegetation was smoothed. Given that hilltops are narrow, we calculated curvature over much smaller spatial scales. We varied the scale from 0.75 m to 5 m to test for scale effects. In Fig. S4 we show four hilltops distributed along the length of DBPR, and the associated variation in C_{HT} and its standard deviation as the scale over which curvature was calculated varied. The selected hilltops are distributed along the length of DBPR, chosen to reflect the various stages in landform development. We observe that C_{HT} varies little with length scales above ~2.5m, except on the sharpest hilltops (Fig. S2(b)) and there is a significant reduction in the standard deviation at this scale. At this scale we see through high frequency noise in the landscape. The hilltop in Fig. S2(b) is extremely narrow and therefore with increasing length scale we are underestimating C_{HT}. This is an important limitation to our results since it alters the range of E^* in Fig. 2, compressing the data at high E^* and may be the cause of clustering. It is therefore possible that any relationship between E and C_{HT} becomes artificially non-linear at high E.

Uplift/Base-level Model

The hillslope model presented in Equation S4 was forward modeled through time, assuming that D = 0.0086 $m^2\ a^{-1}$ (*12*) and L_H = 30 m (Fig. 1), which allowed us to calculate R^* and E^* at each simulated non-dimensional model time (Equation S3d). We favored fixing L_H rather than developing a more complex 2D landscape evolution model to avoid having to model complex valley forming processes, particularly transitions from detachment to transport limited conditions and the initiation of debris-flow processes. Time-dependent dimensionless uplift U^* was idealized as a Gaussian function with duration t_{std}^* peaking at time t_{max}^* and maximum uplift U_{max}^* treated as model parameters:

$$U^* = \frac{2U_{\max}{}^* L_H}{DS_C} e^{-\left(\frac{t^* - t_{\max}{}^*}{t_{std}{}^*}\right)^2} \quad [S7]$$

Posterior probability densities for U^* and $t_{std}{}^*$ were then sampled using a Markov-Chain Monte Carlo (MCMC) method according to the misfit between measured values of R^* and E^* and those calculated at corresponding t^* values in the forward model (*16*) using a maximum likelihood estimator:

$$MLE = \prod_{i=1}^{n} \frac{1}{\sqrt{2\pi}\sigma_u} \exp\left[-\frac{\left(u_i^{meas} - u_i^{\mathrm{mod}}\right)^2}{2\sigma_u{}^2} \right] \quad [S8]$$

where n is the number of data points, u could be either E^* or R^* as a function of time (determined using a space for time substitution based on a fault slip rate of 33 mm yr^{-1}) (*8*), the superscripts *meas* and *mod* denote measured and modeled quantities, respectively, and σ_u is the standard deviation of E^* or R^* data. Values of the peak uplift and width of the Gaussian uplift curve were changed after each iteration of the MCMC 'chain' and then accepted or rejected using an acceptance criterion (see below). For each iteration, the two parameter values were changed from the last accepted parameter value, and this deviation was selected from a Gaussian probability distribution bounded by minimum and maximum parameter values. Following standard practice, the standard deviation of the Gaussian distribution of each parameter (peak uplift and uplift field width) is set so that the acceptance rate of each iteration is c. 33 % (*17*). This process is iterated upon several thousand times in order to constrain the posterior distribution of the model coefficients (*18*). The acceptance criterion is based on the Metropolis-Hastings algorithm (*19*). The likelihood of the current iteration is compared to the previous iteration. If the ratio likelihood of the new iteration to the previous iteration is > 1, then the new coefficient values are accepted. If this ratio is < 1, then the new coefficients are accepted with a probability equal to the ratio. To generate the posterior distribution of coefficient values, each iteration in the Markov Chain is weighted by the likelihood of the combination of parameter values, creating a probability distribution of each coefficient. This can be used to determine both mean and 95% credibility limits on the parameter values. The resulting best fit uplift field can be seen in Fig. 3.

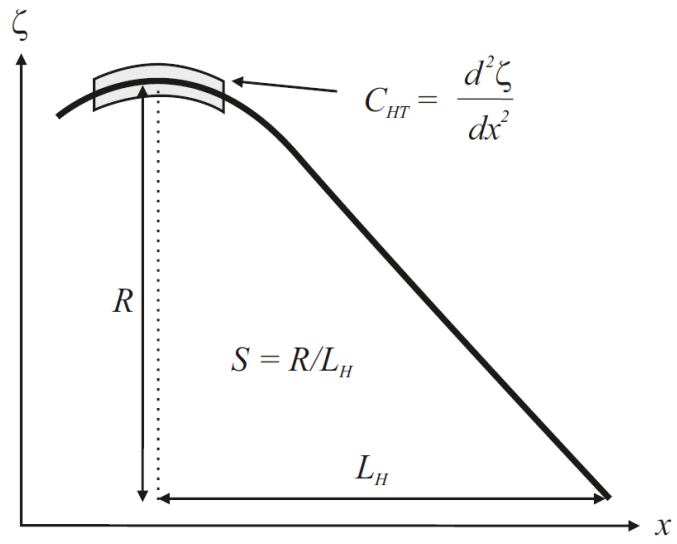

Fig. S1.

One dimensional schematic cross section of a hillslope showing the metrics extracted from topographic data. Relief R is the difference in elevation between the divide and the base of the hillslope, and the horizontal distance between these elevations is the hillslope length L_H. The ratio of these gives the mean hillslope gradient S. Hilltop curvature ($\nabla\zeta$ in 2D space) is the second derivative of the surface measure only at the divide.

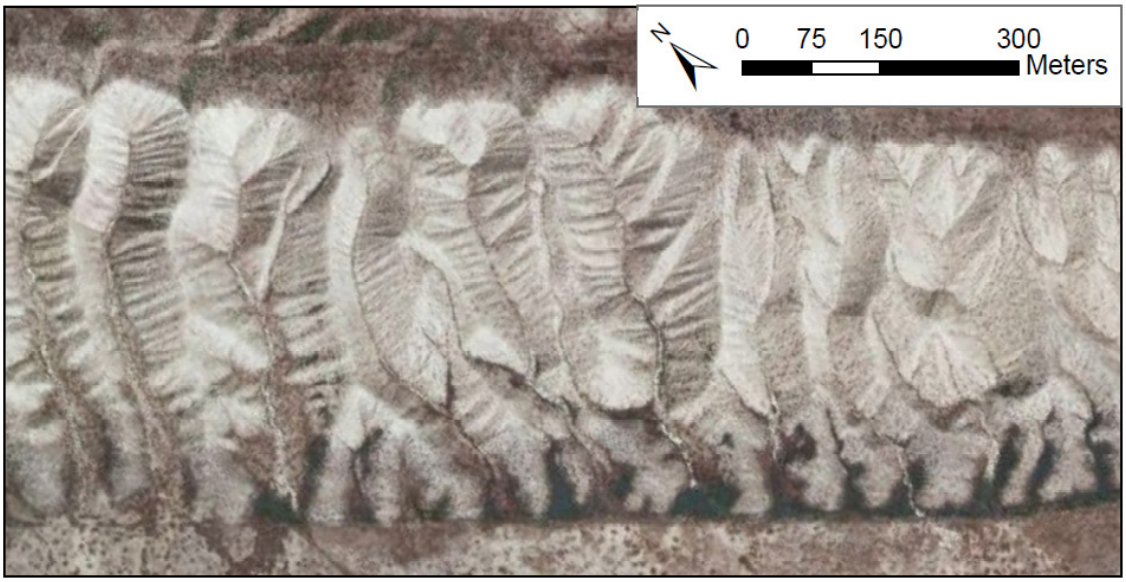

Fig. S2.

Aerial imagary (courtesy of Bing Maps) centered north-west of the zone of high uplift. Note that the hillslopes in this portion of the DBPR are corrugated which is interpreted to be due to small landslides/debris flows. Dark speckles are patchy shrub and brush vegetation which required filtering in the topographic data.

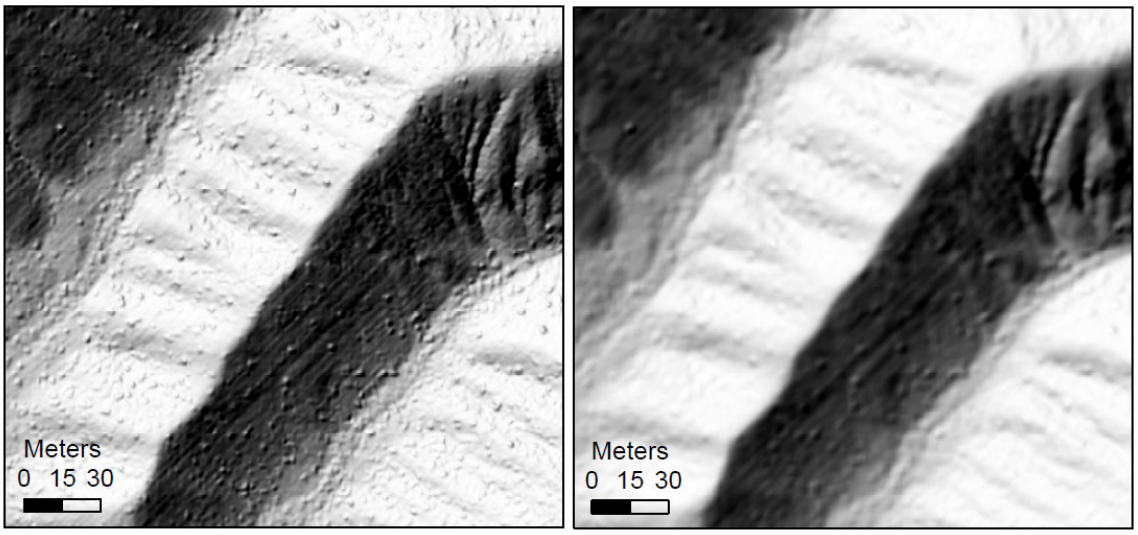

Fig. S3:

Example of smoothing by nonlocal means filtering algorithm which preferentially smoothes positive noise generated by the presence of local surface features such as bushes or boulders. Left image is topographic data gridded to 0.25m, right image is smoothed data using the nonlocal means techniques (*17*).

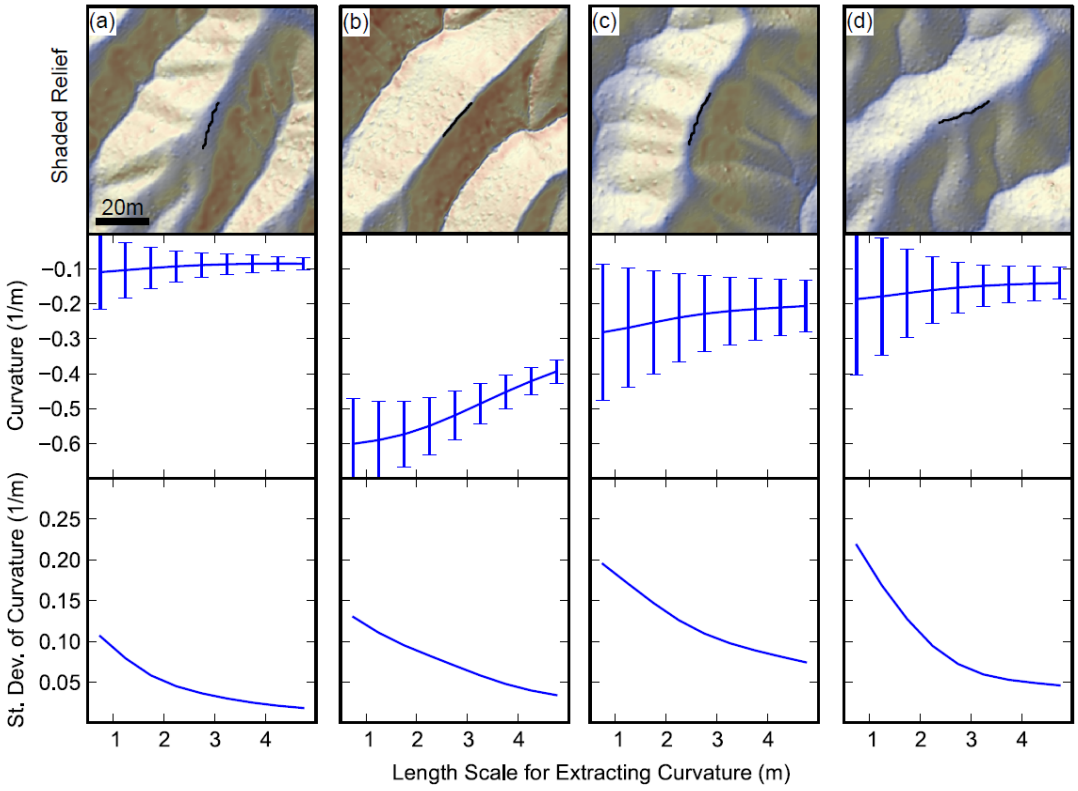

Fig. S4.

Variation in the Hilltop Curvature as a function of the length scale (or window size) over which curvature is extracted from the DEM. For each hilltop depicted in black in the shaded relief image, we extract the mean and standard deviation of curvature with a range of window sizes. Columns (a)-(d) are for hilltops distributed along the length of DBPR recording (a) transient response to uplift/erosion, (b) high erosion rate, steep planar hillslopes and narrow ridges, (c)-(d) relaxation of hillslope after uplift has ceased. For (a), (c) and (d) mean hilltop curvature is independent of window sizes above 2.5m so this is the scale we use. On sharp hilltops with steep side slopes (b) negative hilltop curvature increases as the window size decreases suggesting we will underestimate C_{HT} on such hilltops.

References

1. R. A. DiBiase, A. M. Heimsath, K. X. Whipple, Hillslope response to tectonic forcing in threshold landscapes. *Earth Surf. Process. Landf.* **37**, 855–865 (2012). doi:10.1002/esp.3205

2. M. D. Hurst, S. M. Mudd, R. Walcott, M. Attal, K. Yoo, Using hilltop curvature to derive the spatial distribution of erosion rates. *J. Geophys. Res. Earth Surf.* **117**, F02017 (2012). doi:10.1029/2011JF002057

3. M. D. Hurst, S. M. Mudd, K. Yoo, M. Attal, R. Walcott, Influence of lithology on hillslope morphology and response to tectonic forcing in the northern Sierra Nevada of California. *J. Geophys. Res. Earth Surface* **118**, 832 (2013). doi:10.1002/jgrf.20049

4. A. C. Whittaker, How do landscapes record tectonics and climate? *Lithosphere* **4**, 160–164 (2012). doi:10.1130/RF.L003.1

5. R. A. DiBiase, K. X. Whipple, A. M. Heimsath, W. B. Ouimet, Landscape form and millennial erosion rates in the San Gabriel Mountains, CA. *Earth Planet. Sci. Lett.* **289**, 134–144 (2010). doi:10.1016/j.epsl.2009.10.036

6. S. M. Mudd, D. J. Furbish, Responses of soil-mantled hillslopes to transient channel incision rates. *J. Geophys. Res. Earth Surf.* **112**, F03S18 (2007). doi:10.1029/2006JF000516

7. J. J. Roering, J. T. Perron, J. W. Kirchner, Functional relationships between denudation and hillslope fonn and relief. *Earth Planet. Sci. Lett.* **264**, 245–258 (2007). doi:10.1016/j.epsl.2007.09.035

8. G. E. Hilley, J. R. Arrowsmith, Geomorphic response to uplift along the Dragon's Back pressure ridge, Carrizo Plain. *Calif. Geol.* **36**, 367 (2008). doi:10.1130/G24517A.1

9. S. A. Binnie, W. M. Phillips, M. A. Summerfield, L. K. Fifield, Tectonic uplift, threshold hillslopes, and denudation rates in a developing mountain range. *Geology* **35**, 743 (2007). doi:10.1130/G23641A.1

10. D. J. Andrews, R. C. Bucknam, Fitting degradation of shoreline scarps by a nonlinear diffusion-model. *J. Geophys. Res.* **92**, 12857 (1987). doi:10.1029/JB092iB12p12857

11. J. J. Roering, J. W. Kirchner, W. E. Dietrich, Evidence for nonlinear, diffusive sediment transport on hillslopes and implications for landscape morphology. *Water Resour. Res.* **35**, 853–870 (1999). doi:10.1029/1998WR900090

12. J. R. Arrowsmith, D. D. Rhodes, D. D. Pollard, Morphologic dating of scarps formed by repeated slip events along the San Andreas Fault, Carrizo Plain, California. *J. Geophys. Res.* **103**, 10141 (1998). doi:10.1029/98JB00505

13. J. S. Evans, A. T. Hudak, A multiscale curvature algorithm for classifying discrete return LiDAR in forested environments. Geosci. Remote Sensing *IEEE Trans.* **45**, 1029 (2007).

14. A. Buades, B. Coll, J. M. Morel, A non-local algorithm for image denoising. *Computer Vision Pattern Recognition IEEE Comp. Soc. Conf.* **2**, 60 (2005).

15. R. Jyotsna, P. K. Haff, Microtopography as an indicator of modern hillslope diffusivity in arid terrain. *Geology* **25**, 695 (1997). doi:10.1130/0091-7613(1997)025<0695:MAAIOM>2.3.CO;2

16. N. Metropolis, A. W. Rosenbluth, M. N. Rosenbluth, A. H. Teller, E. Teller, Equation of state calculations by fast computing machines. *J. Chem. Phys.* **21**, 1087 (1953). doi:10.1063/1.1699114

17. A. Gelman, J. B. Carlin, H. S. Stern, D. B. Rubin, *Bayesian Data Analysis* (Chapman and Hall, Xxxxxx, XX, 2003).

18. B. A. Berg, *Introduction to Markov Chain Monte Carlo Simulations and Their Statistical Analysis* (World Scientific, Xxxxxx, XX, 2004).

19. W. K. Hastings, Monte Carlo sampling methods using Markov chains and their applications. *Biometrika* **57**, 97–109 (1970). doi:10.1093/biomet/57.1.97